We are IntechOpen, the world's leading publisher of Open Access books Built by scientists, for scientists

4,800
Open access books available

122,000
International authors and editors

135M
Downloads

Our authors are among the

154
Countries delivered to

TOP 1%
most cited scientists

12.2%
Contributors from top 500 universities

WEB OF SCIENCE™

Selection of our books indexed in the Book Citation Index in Web of Science™ Core Collection (BKCI)

Interested in publishing with us?
Contact book.department@intechopen.com

Numbers displayed above are based on latest data collected.
For more information visit www.intechopen.com

4

Nonlinear Dynamics of Cantilever Tip-Sample Surface Interactions in Atomic Force Microscopy

John H. Cantrell[1] and Sean A. Cantrell[2]
[1]*NASA Langley Research Center*
[2]*Johns Hopkins University*
USA

1. Introduction

The atomic force microscope (AFM) (Bennig et al., 1986) has become an important nanoscale characterization tool for the development of novel materials and devices. The rapid development of new materials produced by the embedding of nanostructural constituents into matrix materials has placed increasing demands on the development of new nanoscale measurement methods and techniques to assess the microstructure-physical property relationships of such materials. Dynamic implementations of the AFM (known variously as acoustic-atomic force microscopies or A-AFM and scanning probe acoustic microscopies or SPAM) utilize the interaction force between the cantilever tip and the sample surface to extract information about sample material properties. Such properties include sample elastic moduli, adhesion, surface viscoelasticity, embedded particle distributions, and topography. The most commonly used A-AFM modalities include various implementations of amplitude modulation-atomic force microscopy (AM-AFM) (including intermittent contact mode or tapping mode) (Zhong et al., 1993), force modulation microscopy (FMM) (Maivald et al., 1991), atomic force acoustic microscopy (AFAM) (Rabe & Arnold, 1994; Rabe et al., 2002), ultrasonic force microscopy (UFM) (Kolosov & Yamanaka, 1993; Yamanaka et al., 1994), heterodyne force microscopy (HFM) (Cuberes et al., 2000; Shekhawat & Dravid, 2005), resonant difference-frequency atomic force ultrasonic microscopy (RDF-AFUM) (Cantrell et al., 2007) and variations of these techniques (Muthuswami & Geer, 2004; Hurley et al., 2003; Geer et al., 2002; Kolosov et al., 1998; Yaralioglu et al., 2000; Zheng et al., 1006; Kopycinska-Müller et al., 2006; Cuberes, 2009).

Central to all A-AFM modalities is the AFM. As illustrated in Fig. 1, the basic AFM consists of a scan head, an AFM controller, and an image processor. The scan head consists of a cantilever with a sharp tip, a piezoelement stack attached to the cantilever to control the distance between the cantilever tip and sample surface (separation distance), and a light beam from a laser source that reflects off the cantilever surface to a photo-diode detector used to monitor the motion of the cantilever as the scan head moves over the sample surface. The output from the photo-diode is used in the image processor to generate the micrograph.

The AFM output signal is derived from the interaction between the cantilever tip and the sample surface. The interaction produces an interaction force that is highly dependent on the

Source: Nonlinear Dynamics, Book edited by: Todd Evans,
ISBN 978-953-7619-61-9, pp. 366, January 2010, INTECH, Croatia, downloaded from SCIYO.COM

tip-sample separation distance. A typical force-separation curve is shown in Fig. 2. Above the separation distance z_A the interaction force is negative, hence attractive, and below z_A the interaction force is positive, hence repulsive. The separation distance z_B is the point on the curve at which the maximum rate of change of the slope of the curve occurs and is thus the point of maximum nonlinearity on the curve (the maximum nonlinearity regime).

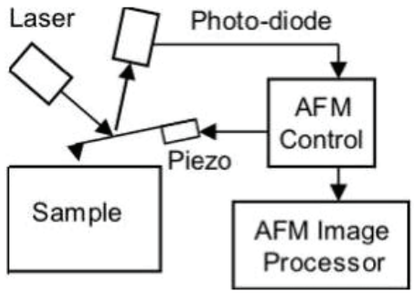

Fig. 1. Schematic of the basic atomic force microscope.

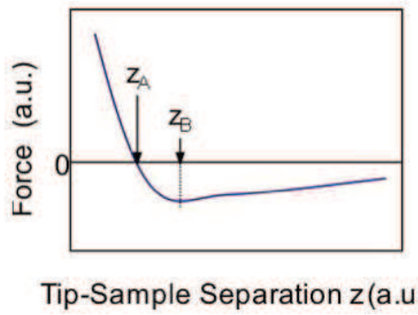

Fig. 2. Interaction force plotted as a function of the separation distance z between cantilever tip and sample surface.

Modalities, such as AFM and AM-AFM, are available for near-surface characterization, while UFM, AFAM, FMM, HFM, and RDF-AFUM are generally used to assess deeper (subsurface) features at the nanoscale. The nanoscale subsurface imaging modalities combine the lateral resolution of the atomic force microscope with the nondestructive capability of acoustic methodologies. The utilization of the AFM in principle provides the necessary lateral resolution for obtaining subsurface images at the nanoscale, but the AFM alone does not enable subsurface imaging. The propagation of acoustic waves through the bulk of the specimen and the impinging of those waves on the specimen surface in contact with the AFM cantilever enable such imaging. The use of acoustic waves in the ultrasonic range of frequencies leads to a more optimal resolution, since both the intensity and the phase variation of waves scattered from nanoscale, subsurface structures increase with increasing frequency (Überall, 1997).

A schematic of the equipment arrangement for the various A-AFM modalities is shown in Fig. 3. The arrangement used for AFAM and FMM is shown in Fig. 3 where the indicated switches are in the open positions. AFAM and FMM utilize ultrasonic waves transmitted into the material by a transducer attached to the bottom of the sample. After propagating through the bulk of the sample, the wave impinges on the sample top surface where it excites the engaged cantilever. For AFAM and FMM the cantilever tip is set to engage the sample surface in hard contact corresponding to the roughly linear interaction region below

z_A of the force-separation curve. The basic equipment arrangement used for UFM is the same as that for AFAM and FMM, except that the cantilever tip for UFM is set to engage the sample in the maximum nonlinearity regime of the force-separation curve. The UFM output signal is a static or "dc" signal resulting from the interaction nonlinearity.

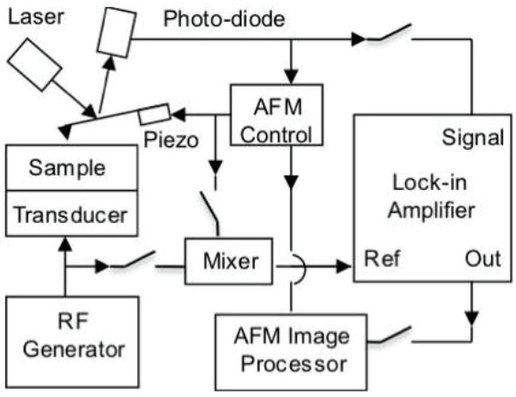

Fig. 3. Acoustic-atomic force microscope equipment configuration. Switches are open for AFAM, FMM, and UFM. Switches are closed for HFM and RDF-AFUM.

The equipment arrangement for RDF-AFUM and HFM is shown in Fig. 3 where the indicated switches are in the closed positions. Similar to the AFAM, FMM and UFM modalities, RDF-AFUM and HFM employ ultrasonic waves launched from the bottom of the sample. However, in contrast to the AFAM, FMM and UFM modalities, the cantilever in RDF-AFUM and HFM is also driven into oscillation. RDF-AFUM and HFM operate in the maximum nonlinearity regime of the force-separation curve, so the nonlinear interaction of the surface and cantilever oscillations produces a strong difference-frequency output signal. For the AM-AFM modality only the cantilever is driven into oscillation and the tip-sample separation distance may be set to any position on the force-separation curve. In one mode of AM-AFM operation the rest or quiescent separation distance z_0 lies well beyond the region of strong tip-sample interaction, i.e. the quiescent separation $z_0 >> z_B$.

Various approaches to assessing the nonlinear behavior of the cantilever probe dynamics have been published (Kolosov & Yamanaka, 1993; Yamanaka et al., 1994; Nony et al., 1999; Yagasaki, 2004; Lee et al., 2006; Kokavecz et al., 2006; Wolf & Gottlieb, 2002; Turner, 2004; Stark & Heckl, 2003; Stark et al., 2004; Hölscher et al., 1999; Garcia & Perez, 2002). We present here a general, yet detailed, analytical treatment of the cantilever and the sample as independent systems in which the nonlinear interaction force provides a coupling between the cantilever tip and the small volume element of sample surface involved in the coupling. The sample volume element is itself subject to a restoring force from the remainder of the sample. We consider only the lowest-order terms in the cantilever tip-sample surface, interaction force nonlinearity. Such terms are sufficient to account for the most important operational characteristics and material properties obtained from each of the various acoustic-atomic force microscopies cited above. A particular advantage of the coupled independent systems model is that the equations are valid for all regions of the force-separation curve and emphasize the local curvature properties (functional form) of the curve. Another advantage is that the dynamics of the sample, hence energy transfer characteristics, can be extracted straightforwardly from the solution set using the same mathematical procedure as that for the cantilever.

We begin by developing a mathematical model of the interaction between the cantilever tip and the sample surface that involves a coupling, via the nonlinear interaction force, of separate dynamical equations for the cantilever and the sample surface. A general solution is found that accounts for the positions of the excitation force (e.g., a piezo-transducer) and the cantilever tip along the length of the cantilever as well as for the position of the laser probe on the cantilever surface. The solution contains static terms (including static terms generated by the nonlinearity), linear oscillatory terms, and nonlinear oscillatory terms. Individual or various combinations of these terms are shown to apply as appropriate to a quantitative description of signal generation for AM-AFM and RDF-AFUM as representatives of the various A-AFM modalities. The two modalities represent opposite extremes in measurement complexity, both in instrumentation and in the analytical expressions used to calculate the output signal. This is followed by a quantitative analysis of image contrast for the A-AFM techniques. As a test of the validity of the present model, comparative measurements of the maximum fractional variation of the Young modulus in a film of LaRC™-CP2 polyimide polymer are presented using the RDF-AFUM and AM-AFM modalities.

2. Analytical model of nonlinear cantilever dynamics

2.1 General dynamical equations

The cantilever of the AFM is able to vibrate in a number of different modes in free space corresponding to various displacement types (flexural, longitudinal, shear, etc.), resonant frequencies, and effective stiffness constants. Although any shape or oscillation mode of the cantilever can in principle be used in the analysis to follow, for definiteness and expediency we consider only the flexural modes of a cantilever modeled as a rectangular, elastic beam of length L, width a, and height b. We assume the beam to be clamped at the position x = 0 and unclamped at the position x = L, as indicated in Fig. 4. We consider the flexural displacement y(x,t) of the beam to be subjected to some general force per unit length H(x,t), where x is the position along the beam and t is time. The dynamical equation for such a beam is

$$E_B I \frac{\partial^4 y(x,t)}{\partial x^4} + \rho_B A_B \frac{\partial^2 y(x,t)}{\partial t^2} = H(x,t) \tag{1}$$

where E_B is the elastic modulus of the beam, $I = ab^3/12$ is the bending moment of inertia, ρ_B is the beam mass density, and $A_B = ab$ is the cross-sectional area of the beam.
The solution to Eq. (1) may be obtained as a superposition of the natural vibrational modes of the unforced cantilever as

$$y(x,t) = \sum_{n=1}^{\infty} Y_n(x)\eta_{cn}(t) \tag{2}$$

where η_{cn} is the nth mode cantilever displacement (n = 1, 2, 3, ···) and the spatial eigenfunctions $Y_n(x)$ form an orthogonal basis set given by (Meirovitch, 1967)

$$Y_n(x) = \left(\frac{\sin q_n x - \sinh q_n x}{\cos q_n x + \cosh q_n x}\right)\left(\sin q_n x - \sinh q_n x\right) + \left(\cos q_n x - \cosh q_n x\right). \tag{3}$$

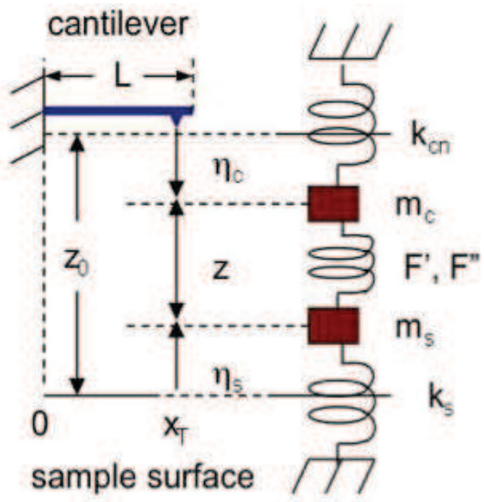

Fig. 4. Schematic of cantilever tip-sample surface interaction: z_0 is the quiescent (rest) tip-surface separation distance (setpoint), z the oscillating tip-surface separation distance, η_c the displacement (positive down) of the cantilever tip, η_s the displacement of the sample surface (positive up), k_{cn} is the nth mode cantilever stiffness constant (represented as an nth mode spring), m_c the cantilever mass, k_s the sample stiffness constant (represented as a single spring), m_s the active sample mass, and $F'(z_0)$ and $F''(z_0)$ are the linear and first-order nonlinear interaction force stiffness constants, respectively, at z_0.

The flexural wave numbers q_n in Eq.(3) are determined from the boundary conditions as $\cos(q_nL)\cosh(q_nL) = -1$ and are related to the corresponding modal angular frequencies ω_n via the dispersion relation $q_n^4 = \omega_n^2 \rho_B A_B / E_B I$. The general force per unit length H(x,t) can also be expanded in terms of the spatial eigenfunctions as (Sokolnikoff & Redheffer, 1958)

$$H(x,t) = \sum_{n=1}^{\infty} B_n(t) Y_n(x) . \tag{4}$$

Applying the orthogonality condition

$$\int_0^L Y_m(x) Y_n dx = L\delta_{mn} \tag{5}$$

(δ_{mn} are the Kronecker deltas) to Eq. (4), we obtain

$$B_n(t) = \int_0^L H(\xi,t) Y_n(\xi) d\xi . \tag{6}$$

We now assume that the general force per unit length acting on the cantilever is composed of (1) a cantilever driving force per unit length $H_c(x,t)$, (2) an interaction force per unit length $H_T(x,t)$ between the cantilever tip and the sample surface, and (3) a dissipative force per unit length $H_d(x,t)$. Thus, the general force per unit length $H(x,t) = H_c(x,t) + H_T(x,t) + H_d(x,t)$. We now assume that the driving force per unit length is a purely sinusoidal oscillation of angular frequency ω_c and magnitude P_c. We also assume the driving force to result from a

drive element (e.g., a piezo-transducer) applied at the point x_c along the cantilever length. We thus write $H_c(x,t) = P_c e^{i\omega_c t}\delta(x - x_c)$ where $\delta(x - x_c)$ is the Dirac delta function. The interaction force per unit length $H_T(x,t)$ of magnitude P_T is applied at the cantilever tip at $x = x_T$ and is not a direct function of time, since it serves as a passive coupling between the independent cantilever and sample systems. We thus write the interaction force per unit length as $H_T(x,t) = P_T\delta(x - x_T)$. We assume the modal dissipation force per unit length $H_d(x,t)$ to be a product of the spatial eigenfunction and the cantilever displacement velocity given as $H_d(x,t) = -P_d Y_n(x)(d\eta_{cn}/dt)$. The coefficient $B_n(t)$ is then obtained from Eq. (6) as

$$B_n(t) = P_c e^{i\omega_c t} Y_n(x_c) + P_T Y_n(x_T) - [P_d \int Y_n(x)dx](d\eta_{cn}/dt) \tag{7}$$

where the integration in the last term is taken over the range x = 0 to x = L. Substituting Eqs. (2) and (4) into Eq.(1) and collecting terms, we find that the dynamics for each mode n must independently satisfy the relation

$$\rho_B A_B Y_n(x)\frac{d^2\eta_{cn}(t)}{dt^2} + E_B I\frac{d^4 Y_n(x)}{dx^4}\eta_{cn} = P_c e^{i\omega_c t} Y_n(x_c) Y_n(x) \tag{8}$$

$$+ P_T Y_n(x_T) Y_n(x) + [P_d \int_0^L Y_n(x)dx]\frac{d\eta_{cn}}{dt}.$$

From Eq. (3) we write $d^4 Y_n/dx^4 = q_n^4 Y_n$. Using this relation and the dispersion relation between q_n and ω_n, we obtain that the coefficient of η_{cn} in Eq.(8) is given by $E_B I(d^4 Y_n/dx^4) = \omega_n^2 \rho_B A_B$. Multiplying Eq. (8) by $Y_m(x)$ and integrating from x = 0 to x = L, we obtain

$$m_c \ddot{\eta}_{cn} + \gamma_c \dot{\eta}_{cn} + k_{cn}\eta_{cn} = F_c e^{i\omega_c t} + F \tag{9}$$

where the overdot denotes derivative with respect to time, $m_c = \rho_B A_B L$ is the total mass of the cantilever and $F_c = P_B L Y_n(x_c)$. The tip-sample interaction force F is defined by $F = P_T L Y_n(x_T)$ and the cantilever stiffness constant k_{cn} is defined by $k_{cn} = m_c \omega_n^2$. The damping coefficient γ_c of the cantilever is defined as $\gamma_c = P_d L \int Y_n(x)dx$. Note that, with regard to the coupled system response, for a given mode n the effective magnitudes of the driving term F_c and the interaction force F are dependent via $Y_n(x_c)$ and $Y_n(x_T)$, respectively, on the positions x_c and x_T at which the forces are applied. The damping factor, in contrast, results from a more general dependence on x via the integral of $Y_n(x)$ over the range zero to L. If the excitation force per unit length is a distributed force over the cantilever surface rather than at a point, then the resulting calculation for F_c would involve an integral over $Y_n(x)$ as obtained for the damping coefficient.

The interaction force F in Eq. (9) is derived without regard to the cantilever tip-sample surface separation distance z. Realistically, the magnitude of F is quite dependent on the separation distance. In particular, various parameters derived from the force-separation curve play an essential role in the response of the cantilever to all driving forces. We further consider that the interaction force not only involves the cantilever at the tip position x_T but

also some elemental volume of material at the sample surface. To maintain equilibrium it is appropriate to view the elemental volume of sample surface as a mass element m_s (active mass) that, in addition to the interaction force, is subjected to a linear restoring force from material in the remainder of the sample. We assume that the restoring force per unit displacement of m_s in the direction z toward the cantilever tip is described by the sample stiffness constant k_s.

The interaction force F between the cantilever tip and the mass element m_s is in general a nonlinear function of the cantilever tip-sample surface separation distance z. A typical nonlinear interaction force F(z) is shown schematically in Fig. 2 plotted as a function of the cantilever tip-sample surface separation distance z. The interaction force results from a number of possible fundamental mechanisms including electrostatic forces, van der Waals forces, interatomic repulsive (e.g., Born-Mayer) potentials, and Casimir forces (Law & Rieutord, 2002; Lantz et al., 2001; Polesel-Maris et al., 2003; Eguchi & Hasegawa, 2002; Saint Jean et al.,; Chan et al., 2001). It is also influenced by chemical potentials as well as hydroxyl groups formed from atmospheric moisture accumulation on the cantilever tip and sample surface (Cantrell, 2004).

Since the force F(z) is common to the cantilever tip and the sample surface element, the cantilever and the sample form a coupled dynamical system. We thus consider the cantilever and the sample as independent dynamical systems coupled by their common interaction force F(z). Fig. 4 shows a schematic representation of the various elements of the coupled system. The dynamical equations expressing the responses of the cantilever and the sample surface to all driving and damping forces may be written for each mode n of the coupled system as

$$m_c\ddot{\eta}_{cn} + \gamma_c\dot{\eta}_{cn} + k_{cn}\eta_{cn} = F(z) + F_c\cos\omega_c t \tag{10}$$

$$m_s\ddot{\eta}_{sn} + \gamma_s\dot{\eta}_{sn} + k_s\eta_{sn} = F(z) + F_s\cos(\omega_s t + \theta) \tag{11}$$

where η_{cn} (positive down) is the cantilever tip displacement for mode n, η_{sn} (positive up) is the sample surface displacement for mode n, ω_c is the angular frequency of the cantilever oscillations, ω_s is the angular frequency of the sample surface vibrations, γ_c is the damping coefficient for the cantilever, γ_s is the damping coefficient for the sample surface, F_c is the magnitude of the cantilever driving force, F_s is the magnitude of the sample driving force that we assume here to result from an incident ultrasonic wave generated at the opposite surface of the sample. The factor θ is a phase contribution resulting from the propagation of the ultrasonic wave through the sample material and is considered in more detail in Section 2.2.

Eqs. (10) and (11) are coupled equations representing the cantilever tip-sample surface dynamics resulting from the nonlinear interaction forces. The equations govern the cantilever and surface displacements η_{cn} and η_{sn}, respectively at $x = x_T$. In a realistic AFM measurement of the cantilever response to the driving forces, the measurement point is not generally at $x = x_T$, but at the point $x = x_L$ at which the laser beam of the AFM optical detector system strikes the cantilever surface. The cantilever response at $x = x_L$ is found from Eq. (2) to be

$$y(x_L, t) = \eta_c(t) = \sum_{n=1}^{\infty} Y_n(x_L)\eta_{cn}(t) \tag{12}$$

We note from Fig. 4 that for a given mode n, $z = z_o - (\eta_{cn} + \eta_{sn})$, where z_0 is the quiescent separation distance between the cantilever tip and the sample surface (setpoint distance). We use this relationship in a power series expansion of $F(z)$ about z_o to obtain

$$F(z) = F(z_0) + F'(z_0)(z - z_0) + \frac{1}{2}F''(z_0)(z - z_0)^2 + \cdots \tag{13}$$

$$= F(z_0) - F'(z_0)(\eta_{cn} + \eta_{sn}) + \frac{1}{2}F''(z_0)(\eta_{cn} + \eta_{sn})^2 + \cdots$$

where the prime denotes derivative with respect to z. Substitution of Eq. (13) into Eqs. (10) and (11) gives

$$m_c\ddot{\eta}_{cn} + \gamma_c\dot{\eta}_{cn} + [k_{cn} + F'(z_0)]\eta_{cn} + F'(z_0)\eta_{sn} = F(z_0) + F_c\cos\omega_c t \tag{14}$$

$$+ \frac{1}{2}F''(z_0)(\eta_{cn} + \eta_{sn})^2 + \cdots$$

$$m_s\ddot{\eta}_{sn} + \gamma_s\dot{\eta}_{sn} + [k_s + F'(z_0)]\eta_{sn} + F'(z_0)\eta_{cn} = F(z_0) + F_s\cos(\omega_s t + \theta) \tag{15}$$

$$+ \frac{1}{2}F''(z_0)(\eta_{cn} + \eta_{sn})^2 + \cdots.$$

It is of interest to note that Eqs. (14) and (15) were obtained assuming that the cantilever is a rectangular beam of constant cross-section. Such a restriction is not necessary, since the mathematical procedure leading to Eqs. (14) and (15) is based on the assumption that the general displacement of the cantilever can be expanded in terms of a set of eigenfunctions that form an orthogonal basis set for the problem. For the beam cantilever the eigenfunctions are $Y_n(x)$. For some other cantilever shape a different orthogonal basis set of eigenfunctions would be appropriate. However, the mathematical procedure used here would lead again to Eqs. (14) and (15) with values of the coefficients appropriate to the different cantilever geometry.

2.2 Variations in signal amplitude and phase from subsurface features

We consider a traveling stress wave of unit amplitude of the form $e^{-\alpha x}\cos(\omega_s t - kx) = \mathrm{Re}[e^{-\alpha x}e^{i(\omega_s t - kx)}]$, where α is the attenuation coefficient, x is the propagation distance, ω_s is the angular frequency, t is time, $k = \omega_s / c$, and c is the phase velocity, propagating through a sample of thickness a/2. We assume that the wave is generated at the bottom surface of the sample at the position x = 0 and that the wave is reflected between the top and bottom surfaces of the sample. We assume that the effect of the reflections is simply to change the direction of wave propagation.

For continuous waves the complex waveform at a point x in the material consists of the sum of all contributions resulting from waves which had been generated at the point x = 0 and have propagated to the point x after multiple reflections from the sample boundaries. We thus write the complex wave $\overline{A}(t)$ as

$$\overline{A}(t) = e^{-\alpha x} e^{i(\omega_s t - kx)} [1 + e^{-(\alpha a + ika)} + \cdots + e^{-n(\alpha a + ika)} + \cdots]$$

$$= e^{-\alpha x} e^{i(\omega_s t - kx)} \sum_{n=0}^{\infty} \left[e^{-(\alpha a + ika)} \right]^{-n} = e^{-\alpha x} e^{i(\omega_s t - kx)} \frac{1}{1 - e^{-(\alpha a + ika)}} \tag{16}$$

where the last equality follows from the geometric series generated by the infinite sum. The real waveform A(t) is obtained from Eq. (16) as

$$A(t) = \mathrm{Re}[\overline{A}(t)] = e^{-\alpha x} (A_1^2 + A_2^2)^{1/2} \cos(\omega_s t - kx - \phi) = e^{-\alpha x} B \cos(\omega_s t - kx - \phi) \tag{17}$$

where

$$A_1 = \frac{e^{\alpha a} - \cos ka}{2(\cosh \alpha a - \cos ka)}, \tag{18}$$

$$A_2 = -\frac{\sin ka}{2(\cosh \alpha a - \cos ka)}, \tag{19}$$

$$\phi = \tan^{-1} \frac{\sin ka}{e^{\alpha a} - \cos ka}, \tag{20}$$

and

$$B = (A_1^2 + A_2^2)^{1/2} = (1 + e^{-2\alpha a} - 2e^{-\alpha a} \cos ka)^{-1/2}. \tag{21}$$

The evaluation (detection) of a continuous wave at the end of the sample opposite that of the source is obtained by setting x = a/2 in the above equations. It is at x = a/2 that the AFM cantilever engages the sample surface. In the following equations we set x = a/2.

The above results are derived for a homogeneous specimen. Consider now that the specimen of thickness a/2 having phase velocity c contains embedded material of thickness d/2 having phase velocity c_d. The phase factor $ka = \omega_s a / c$ in Eqs.(17)-(21) must then be replaced by ka - ψ where

$$\psi = \omega_s d \left(\frac{1}{c} - \frac{1}{c_d} \right) = \omega_s d \frac{\Delta c}{c_d c} = kd \frac{\Delta c}{c_d} \tag{22}$$

and $\Delta c = c_d - c$. We thus set x = a/2 and re-write Eqs.(17), (20), and (21) as

$$A'(t) = e^{-\alpha a/2} B' \cos[\omega_s t - \frac{(ka - \psi)}{2} - \phi'] \tag{23}$$

where

$$\phi' = \tan^{-1} \frac{\sin(ka - \psi)}{e^{\alpha a} - \cos(ka - \psi)}, \tag{24}$$

and

$$B' = [1 + e^{-2\alpha a} - 2e^{-\alpha a}\cos(ka - \psi)]^{-1/2}. \quad (25)$$

We have assumed in obtaining the above equations that the change in the attenuation coefficient resulting from the embedded material is negligible.

For small ψ we may expand Eq. (23) in a power series about $\psi = 0$. Keeping only terms to first order, we obtain

$$\phi' = \phi + \Delta\phi \quad (26)$$

where

$$\Delta\phi = -\psi\left[\frac{e^{\alpha a}\cos ka - 1}{(e^{\alpha a} - \cos ka)^2 + \sin^2 ka}\right]. \quad (27)$$

Eq.(22) is thus approximated as

$$A'(t) = e^{-\alpha a/2}B'\cos(\omega_s t - \frac{ka}{2} - \phi + \frac{\psi}{2} - \Delta\phi) = e^{-\alpha a/2}B'\cos(\omega_s t + \theta) \quad (28)$$

where

$$\theta = -(\chi + \Delta\chi) = -\left(\frac{ka}{2} + \phi - \frac{\psi}{2} + \Delta\phi\right), \quad (29)$$

$$\chi = \frac{ka}{2} + \phi \quad (30)$$

and

$$\Delta\chi = -\frac{\psi}{2} + \Delta\phi = -\psi\left[\frac{1}{2} + \frac{e^{\alpha a}\cos ka - 1}{(e^{\alpha a} - \cos ka)^2 + \sin^2 ka}\right]. \quad (31)$$

Equation (28) reveals that the total phase contribution at x = a/2 is θ and from Eqs.(29) and (31) that the phase variation resulting from embedded material is $-\Delta\chi$.

The fractional change in the Young modulus $\Delta E/E$ is related to the fractional change in the ultrasonic longitudinal velocity $\Delta c/c$ as $\Delta E/E \approx \Delta C_{11}/C_{11} = (2\Delta c/c) + (\Delta\rho/\rho)$ where ρ is the mass density of the sample and C_{11} is the Brugger longitudinal elastic constant. Assuming that the fractional change in the mass density is small compared to the fractional change in the wave velocity, we may estimate the relationship between $\Delta E/E$ and $\Delta c/c$ as $\Delta E/E \approx 2\Delta c/c$. This relationship may be used to express ψ, given in Eq.(22) in terms of $\Delta c/c_d = (c/c_d)(\Delta c/c)$, in terms of $\Delta E/E$.

2.3 Solution to the general dynamical equations

We solve the coupled nonlinear Eqs. (14) and (15) for the steady-state solution by writing the coupled equations in matrix form and using an iteration procedure commonly employed in the physics literature (Schiff, 1968) to solve the matrix expression. The first iteration involves solving the equations for which the nonlinear terms are neglected. The second iteration is obtained by substituting the first iterative solution into the nonlinear terms of Eqs.(14) and

(15) and solving the resulting equations. The procedure provides solutions both for the cantilever tip and the sample surface displacements. Since the procedure is much too lengthy to reproduce here in full detail, only the salient features of the procedure leading to the steady state solution for the cantilever displacement $\eta_c = \sum Y_n \eta_{cn}$ are given. We begin by writing

$$\eta_{cn} = \varepsilon_{cn} + \xi_{cn} + \zeta_{cn} \tag{32}$$

and

$$\eta_{sn} = \varepsilon_{sn} + \xi_{sn} + \zeta_{sn} \tag{33}$$

where ε_{cn} and ξ_{cn} represent the first iteration (i.e. linear) static and oscillatory solutions, respectively, for the nth mode cantilever displacement, ζ_{cn} represents the second iteration (i.e., nonlinear) solution for the nth mode cantilever displacement, and ε_{sn} , ξ_{sn} , and ζ_{sn} are the corresponding first and second iteration nth mode displacements for the sample surface.

We note that for the range of frequencies generally employed in A-AFM the contribution from terms in the solution set involving the mass of the sample element m_s is small compared to the remaining terms and may to an excellent approximation be neglected. We thus neglect the terms involving m_s in the following equations.

2.3.1 First iterative solution

The first iterative solution is obtained by linearizing Eqs.(14) and (15), writing the resulting expression in matrix form, and solving the matrix expression assuming sinusoidal driving terms $F_c e^{i\omega_c t}$ and $F_s e^{i\omega_s t}$ for the cantilever and sample surface, respectively. The first iteration yields a static solution ε_{cn} and an oscillatory solution ξ_{cn} for the cantilever. The static solution is given by

$$\varepsilon_{cn} = \frac{k_s F(z_o)}{k_{cn}k_s + F'(z_o)(k_{cn} + k_s)}. \tag{34}$$

The first iterative oscillatory solution is given by

$$\xi_{cn} = Q_{cc}\cos(\omega_c t + \alpha_{cc} - \phi_{cc}) + Q_{cs}\cos(\omega_s t - \phi_{ss} + \theta) \tag{35}$$

where

$$\phi_{cc} \approx \tan^{-1}\frac{(\gamma_c k_s + \gamma_s k_{cn})\omega_c - \gamma_s m_c \omega_c^3 + F'(z_0)(\gamma_c + \gamma_s)\omega_c}{k_{cn}k_s - (m_c k_s + \gamma_c\gamma_s)\omega_c^2 + F'(z_0)(k_{cn} + k_s - m_c\omega_c^2)}, \tag{36}$$

$$\phi_{ss} \approx \tan^{-1}\frac{(\gamma_c k_s + \gamma_s k_{cn})\omega_s - \gamma_s m_c \omega_s^3 + F'(z_0)(\gamma_c + \gamma_s)\omega_s}{k_{cn}k_s - (m_c k_s + \gamma_c\gamma_s)\omega_s^2 + F'(z_0)(k_{cn} + k_s - m_c\omega_s^2)}, \tag{37}$$

$$Q_{cc} \approx F_c\{[k_s + F'(z_o)]^2 + \gamma_s^2\omega_c^2\}^{1/2}\{[k_{cn}k_s - \omega_c^2(m_c k_s + \gamma_c\gamma_s)$$

$$+F'(z_o)(k_{cn} + k_s - m_c\omega_c^2)]^2 + [\omega_c(\gamma_s k_{cn} + \gamma_c k_s) \tag{38}$$

$$-\omega_c^3\gamma_s m_c + F'(z_o)\omega_c(\gamma_s+\gamma_c)]^2\}^{-1/2},$$

and

$$Q_{cs} \approx -F_s F'(z_o)\{[k_{cn}k_s - \omega_s^2(m_c k_s + \gamma_c\gamma_s) + F'(z_o)(k_{cn}+k_s - m_c\omega_s^2)]^2 \tag{39}$$

$$+[\omega_s(\gamma_s k_{cn} + \gamma_c k_s) - \omega_s^3\gamma_s m_c + F'(z_o)\omega_s(\gamma_s+\gamma_c)]^2\}^{-1/2}.$$

2.3.2 Second iterative solution

The second iterative solution ζ_{cn} for each mode n of the cantilever is considerably more complicated, since it contains not only sum-frequency, difference-frequency, and generated harmonic-frequency components, but linear and static components as well. The second iterative solution ζ_{cn} is thus written as

$$\zeta_{cn} = \zeta_{cn,stat} + \zeta_{cn,lin} + \zeta_{cn,diff} + \zeta_{cn,sum} + \zeta_{cn,harm} \tag{40}$$

where $\zeta_{cn,stat}$ is a static or "dc" contribution generated by the nonlinear tip-surface interaction, $\zeta_{cn,lin}$ is a generated linear oscillatory contribution, $\zeta_{cn,diff}$ is a generated difference-frequency contribution resulting from the nonlinear mixing of the cantilever and sample oscillations, $\zeta_{cn,sum}$ is a generated sum-frequency contribution resulting from the nonlinear mixing of the cantilever and sample oscillations, and $\zeta_{cn,harm}$ are generated harmonic contributions.

Generally, the cantilever responds with decreasing displacement amplitudes as the drive frequency is increased above the fundamental resonance (for some cantilevers the second resonance mode has the largest amplitude), even when driven at higher modal frequencies. Thus, acoustic-atomic force microscopy methods do not generally utilize harmonic or sum-frequency signals. For expediency, such signals from the second iteration will not be considered here. Only the static, linear, and difference-frequency terms from the second iteration solution are relevant to the most commonly used A-AFM modalities.

The static contribution generated by the nonlinear interaction force is obtained to be

$$\zeta_{cn,stat} = \frac{1}{4}\frac{k_s F''(z_o)}{[k_{cn}k_s + F'(z_o)(k_{cn}+k_s)]}[2\varepsilon_o^2 + Q_{cc}^2 + Q_{cs}^2 + Q_{sc}^2 + Q_{ss}^2 \tag{41}$$

$$+2Q_{cc}Q_{sc}\cos(\alpha_{cc} - 2\phi_{cc}) + 2Q_{cs}Q_{ss}\cos\alpha_{ss}]$$

where

$$\varepsilon_o = \frac{(k_{cn}+k_s)F(z_o)}{k_{cn}k_s + F'(z_o)(k_{cn}+k_s)}, \tag{42}$$

$$Q_{sc} \approx -F_c F'(z_o)\{[k_{cn}k_s - \omega_c^2(m_c k_s + \gamma_c\gamma_s) + F'(z_o)(k_{cn}+k_s - m_c\omega_c^2)]^2 \tag{43}$$

$$+[\omega_c(\gamma_s k_{cn} + \gamma_c k_s) - \omega_c^3\gamma_s m_c + F'(z_o)\omega_c(\gamma_s+\gamma_c)]^2\}^{-1/2},$$

$$Q_{ss} \approx F_s\{[k_s + F'(z_o)]^2 + \gamma_s^2\omega_s^2\}^{1/2}\{[k_{cn}k_s - \omega_s^2(m_c k_s + \gamma_c\gamma_s) \tag{44}$$

$$+F'(z_o)(k_{cn}+k_s-m_c\omega_s^2)]^2+[\omega_s(\gamma_s k_{cn}+\gamma_c k_s)$$

$$-\omega_s^3\gamma_s m_c+F'(z_o)\omega_c(\gamma_s+\gamma_c)]^2\}^{-1/2},$$

$$\alpha_{cc}=\tan^{-1}\frac{\gamma_s\omega_c}{k_s+F'(z_o)}, \tag{45}$$

$$\alpha_{ss}=\tan^{-1}\frac{\gamma_c\omega_s}{k_{cn}+F'(z_o)-m_c\omega_s^2} \tag{46}$$

and ϕ_{cc} is given by Eq. (36), Q_{cc} by Eq. (38) and Q_{cs} by Eq.(39).
The linear oscillatory contribution $\zeta_{cn,lin}$ generated by the nonlinear interaction force in the second iteration is obtained to be

$$\zeta_{cn,lin}=\frac{D_c}{R_{cc}}\varepsilon_o F''(z_o)[Q_{cc}^2+Q_{sc}^2+2Q_{cc}Q_{sc}\cos\alpha_{cc}]^{1/2}\cos(\omega_c t-2\phi_{cc}+\beta_c+\mu_{cc}) \tag{47}$$

$$+\frac{D_s}{R_{ss}}\varepsilon_o F''(z_o)[Q_{ss}^2+Q_{cs}^2+2Q_{ss}Q_{cs}\cos\alpha_{ss}]^{1/2}\cos(\omega_s t-2\phi_{ss}+\beta_s+\mu_{ss}+\theta)$$

where

$$\mu_{cc}=\tan^{-1}\frac{Q_{cc}\sin\alpha_{cc}}{Q_{cc}\cos\alpha_{cc}+Q_{sc}}, \tag{48}$$

$$\mu_{ss}=\tan^{-1}\frac{Q_{ss}\sin\alpha_{ss}}{Q_{ss}\cos\alpha_{ss}+Q_{cs}}, \tag{49}$$

$$\beta_c=\tan^{-1}\frac{\gamma_s\omega_c}{k_s}, \tag{50}$$

$$\beta_s=\tan^{-1}\frac{\gamma_s\omega_s}{k_s}, \tag{51}$$

$$D_c=[k_s^2+\gamma_s^2\omega_c^2]^{1/2}, \tag{52}$$

$$D_s=[k_s^2+\gamma_s^2\omega_s^2]^{1/2}, \tag{53}$$

$$R_{ss}=\{[k_{cn}k_s-\omega_s^2(m_c k_s+\gamma_c\gamma_s)+F'(z_o)(k_{cn}+k_s-m_c\omega_s^2)]^2 \tag{54}$$

$$+[\omega_s(\gamma_s k_{cn}+\gamma_c k_s)-\gamma_s m_c\omega_s^3+F'(z_o)\omega_s(\gamma_s+\gamma_c)]^2\}^{1/2},$$

and

$$R_{cc}=\{[k_{cn}k_s-\omega_c^2(m_c k_s+\gamma_c\gamma_s)+F'(z_o)(k_{cn}+k_s-m_c\omega_c^2)]^2 \tag{55}$$

$$+[\omega_c(\gamma_s k_{cn}+\gamma_c k_s)-\gamma_s m_c\omega_c^3+F'(z_o)\omega_c(\gamma_s+\gamma_c)]^2\}^{1/2}.$$

The difference-frequency contribution $\zeta_{cn,diff}$ generated by the nonlinear interaction force in the second iteration is obtained to be

$$\zeta_{cn,diff}=G_n\cos[(\omega_c-\omega_s)t-\phi_{cc}+\phi_{ss}+\beta_{cs}-\phi_{cs}+\Gamma-\theta] \tag{56}$$

where

$$G_n=\frac{1}{2}\frac{D_{cs}}{R_{cs}}F''(z_o)\{Q_{cc}^2Q_{cs}^2+Q_{sc}^2Q_{ss}^2+Q_{cc}^2Q_{ss}^2+Q_{cs}^2Q_{sc}^2 \tag{57}$$

$$+2Q_{cc}Q_{cs}Q_{sc}Q_{ss}\cos(\alpha_{cc}+\alpha_{ss})+2Q_{cc}^2Q_{cs}Q_{ss}\cos\alpha_{ss}+2Q_{cc}Q_{cs}^2Q_{sc}\cos\alpha_{cc}$$

$$+2Q_{sc}^2Q_{ss}Q_{cs}\cos\alpha_{ss}+2Q_{cc}Q_{ss}Q_{cs}Q_{sc}\cos(\alpha_{cc}-\alpha_{ss})\}^{1/2},$$

$$D_{cs}=\sqrt{k_s^2+\gamma_s^2(\omega_c-\omega_s)^2}\,, \tag{58}$$

$$R_{cs}=\sqrt{R_{cs1}^2+R_{cs2}^2}\,, \tag{59}$$

$$R_{cs1}=k_{cn}k_s-m_ck_s(\omega_c-\omega_s)^2-\gamma_c\gamma_s(\omega_c-\omega_s)^2+F'(z_o)[k_{cn}+k_s-m_c(\omega_c-\omega_s)^2], \tag{60}$$

$$R_{cs2}=(\omega_c-\omega_s)(\gamma_s k_c+\gamma_c k_s)-\gamma_s m_c(\omega_c-\omega_s)^3+F'(z_o)(\omega_c-\omega_s)(\gamma_s+\gamma_c), \tag{61}$$

$$\phi_{cs}=\tan^{-1}\frac{R_{cs2}}{R_{cs1}} \tag{62}$$

$$\approx\tan^{-1}\frac{(\gamma_c k_s+\gamma_s k_{cn})(\omega_c-\omega_s)-\gamma_s m_c(\omega_c-\omega_s)^3+F'(z_0)(\gamma_c+\gamma_s)(\omega_c-\omega_s)}{k_{cn}k_s-(m_ck_s+\gamma_c\gamma_s)(\omega_c-\omega_s)^2+F'(z_0)[k_{cn}+k_s-m_c(\omega_c-\omega_s)^2]},$$

$$\beta_{cs}=\tan^{-1}\frac{\gamma_s(\omega_c-\omega_s)}{k_s}, \tag{63}$$

and

$$\Gamma=\tan^{-1}\frac{Q_{cc}Q_{cs}\sin\alpha_{cc}-Q_{sc}Q_{ss}\sin\alpha_{ss}+Q_{cc}Q_{ss}\sin(\alpha_{cc}-\alpha_{ss})}{Q_{cc}Q_{cs}\cos\alpha_{cc}+Q_{sc}Q_{ss}\cos\alpha_{ss}+Q_{cc}Q_{ss}\cos(\alpha_{cc}-\alpha_{ss})+Q_{cs}Q_{sc}}. \tag{64}$$

The phase term Γ given by Eq.(64) is quite complicated. However, advantage can be taken of the fact that k_s is generally large compared to other terms in the numerators of Q_{cc}, Q_{ss}, Q_{cs}, and Q_{sc}; the denominators of these terms are very roughly all equal. Hence, the magnitudes of Q_{cc} and Q_{ss} are usually large compared to those of Q_{cs} and Q_{sc}. The terms involving the product $Q_{cc}Q_{ss}$ thus dominate in Eq. (64) and we may approximate Γ as

$$\Gamma \approx \alpha_{cc} - \alpha_{ss} = \tan^{-1}\frac{\gamma_s \omega_c}{k_s + F'(z_0)} - \tan^{-1}\frac{\gamma_c \omega_s}{k_{cn} + F'(z_0) - m_c \omega_s^2} \tag{65}$$

where α_{cc} and α_{ss} are obtained from Eqs. (45) and (46), respectively. To the same extent that Γ may be approximated by Eq.(65) we may also approximate G_n, given by Eq. (57), as

$$G_n \approx \frac{F''(z_0)}{2}\frac{D_{cs}}{R_{cs}} Q_{cc} Q_{ss} \,. \tag{66}$$

2.3.3 Important features of the solution set

The present derivation is based on the assumption that the cantilever tip-sample surface interaction force is a multiply differentiable, nonlinear function of the tip-surface separation distance as indicated in Fig. 2. Points on the curve below the separation distance z_A in Fig. 2 correspond to a repulsive interaction force, while points above z_A in Fig. 2 correspond to an attractive interaction force. The force-separation curve has a minimum at a separation distance z_B corresponding to the maximum nonlinearity of the curve and that point lies in the attractive force portion of the curve. Cantilever oscillations result in continuous oscillatory changes in the tip-surface separation distance about the quiescent tip-surface separation distance z_0 (see Fig. 4). Since the cantilever oscillations are constrained to follow the force-separation curve, the fractions of the cantilever oscillation cycle in the repulsive and attractive portions of the force-separation curve depend on the quiescent tip-surface separation distance and the amplitude of the oscillations.

The cantilever oscillations are known to be bi-stable with the particular mode of oscillation being determined by the initial conditions that includes the tip-surface separation distance (Garcia & Perez, 2002). Unless some extraneous perturbation changes the mode of oscillation, the cantilever continues to oscillate in a given bi-stable mode for a given set of initial conditions. For large oscillation amplitudes the bi-stability coalesces to a single stable mode. In the present model the bi-stable mode of cantilever oscillation is set by the value of the "effective" sample stiffness constant k_s that has one of two values – one associated with the dominantly repulsive portion of the force-separation curve and one associated with the dominantly attractive portion (see Section 4.3). The value of the "effective" sample stiffness constant, hence cantilever oscillation mode, must be determined experimentally in the present model.

The total static solution to the coupled nonlinear equations (14) and (15) for the cantilever $\eta_{cn,stat}$ is the sum of the contribution ε_{cn}, given by Eq. (34), from the first iterative solution and the contribution $\zeta_{cn,stat}$, given by Eq. (41), from the second iteration as

$$\eta_{cn,stat} = \varepsilon_{cn} + \zeta_{cn,stat} \,. \tag{67}$$

The total linear solution $\eta_{cn,lin}$ to Eqs. (14) and (15) is the sum of the contribution ξ_{cn} given by Eq. (35) and the contribution $\zeta_{cn,lin}$ given by Eq. (47) as

$$\eta_{cn,lin} = \xi_{cn} + \zeta_{cn,lin} \,. \tag{68}$$

The total difference-frequency solution $\eta_{cn,diff}$ to Eqs. (14) and (15) is simply the contribution $\zeta_{cn,diff}$ given by Eq. (56).

It is interesting to note that ε_{cn} and the component ε_o in $\eta_{cn,stat}$ do not explicitly involve the cantilever drive amplitude F_c and the sample surface drive amplitude F_s, although other terms involving the Q factors, given by Eqs. (38), (39), (43), and (44), in $\zeta_{cn,stat}$ do involve these drive amplitudes. This means that only the contributions stemming from the nonlinearity in the cantilever tip-sample surface interaction force respond directly to variations in the drive amplitudes and in particular to the physical features of the material giving rise to variations in F_s. Further, the magnitudes of all second iteration (i.e. nonlinear) contributions, $\zeta_{cn,stat}$, $\zeta_{cn,lin}$, and $\zeta_{cn,diff}$ are strongly dependent on the cantilever tip-sample surface quiescent separation z_o, since the value of the nonlinear stiffness constant $F''(z_o)$ that dominates these contributions is highly sensitive to z_o. Indeed, $F''(z_o)$ attains a maximum value near the bottom of the force-separation curve of Fig. 2.

For large deflections of the cantilever that may occur for sufficiently hard contact, large bending moments may be introduced that produce frequency shifts in the cantilever resonance frequencies quite apart from those introduced by the interaction force stiffness constant $F'(z_0)$. For the assessment of $F'(z_0)$ near the bottom of the force-separation curve where the nonlinearity $F''(z_0)$ is maximum (maximum nonlinearity regime) and $F'(z_0)$ is relatively small, the bending moments are generally negligible and a reasonable estimate of $F'(z_0)$ can be obtained directly from differences in the engaged and non-engaged resonance (free space) frequencies of the cantilever.

For large driving force amplitudes, nonlinear modes of oscillation may be generated in the cantilever. Nonlinear tip-surface interactions are also known to excite nonlinear (anharmonic) cantilever modes (Stark & Heckl, 2003; Garcia & Perez, 2002). It is assumed that the nonlinear modes can be described in terms of a set of orthogonal eigenfunctions $Z_n(x)$ describing the nonlinearities of the unforced cantilever that are generally different from but orthogonal to $Y_n(x)$. In such case the nonlinear vibrational characteristics of the cantilever may also be included in the general cantilever response in a manner similar to that given above for the linear modes. The nonlinear modes are thus formally included in the present model by extending the set of eigenvalues k_{cn}, hence eigenvectors spanning the function space, to allow for nonlinear eigenmodes. This requires no additional formal analysis in the present model. All eigenvalues (including those from nonlinear modes) are ascertained in the present model from experimental measurements.

3. Signal generation for representative A-AFM modalities

Generally, there are two working modes in A-AFM - the contact mode and the non-contact mode. The contact mode is viewed as a modality for which the oscillating cantilever tip makes periodic contact with the sample surface irrespective of the distance of separation (setpont distance) between the non-oscillating (quiescent) cantilever tip and the sample surface. When the setpoint distance z_0 lies close to the sample surface, the cantilever operates near the dominantly repulsive portion of the cantilever tip-sample surface interaction force-separation curve and experiences a dominantly repulsive force over some appreciable fraction of an oscillation period (contact time). The oscillation amplitude is usually small for this contact mode of operation and the tip-surface interaction force may be approximated by a linear dependence of the tip-surface interaction force on the tip-surface separation distance. A-AFM modalities that operate in the contact mode include force

modulation microscopy, atomic force acoustic microscopy, and a modality of amplitude modulation-atomic force microscopy (AM-AFM) that may be descriptively called 'small amplitude contact tapping mode.'

Various other A-AFM modalities operate in the non-contact mode where the cantilever tip-sample surface setpoint distance z_0 is sufficiently large that the cantilever tip, oscillating with small amplitude, does not contact with the sample surface. In such cases the modalities optimally operate in that portion of the force-separation curve that yields the maximum force-separation nonlinearity, appropriately called the 'maximum nonlinearity regime' of A-AFM operation. Ultrasonic force microscopy, heterodyne force microscopy, and resonant difference-frequency atomic force ultrasonic microscopy (RDF-AFUM) are examples of non-contact A-AFM modalities. Non-contact amplitude modulation-atomic force microscopy (noncontact tapping mode) also operates in this portion of the force-separation curve.

The equations derived in Section 2, describing the dynamical response of the cantilever resulting from the cantilever tip-sample surface interaction forces, have been used to quantify the signal generation and image contrast for all A-AFM modalities mentioned in the introduction (Cantrell & Cantrell, 2008). We consider here, however, only resonant difference-frequency atomic force ultrasonic microscopy (RDF-AFUM), and the commonly used amplitude modulation-atomic force microscopy (AM-AFM), a modality that includes the intermittent contact mode as well as contact and non-contact tapping modes. RDF-AFUM and AM-AFM represent opposite extremes in complexity, both in instrumentation and in the analytical expressions used to assess signal generation and image contrast.

RDF-AFUM uses input drive oscillations both to the cantilever and to the sample surface to interrogate the sample. It is the most complex of the A-AFM modalities and the assessment of signal generation and image contrast for RDF-AFUM requires application of the largest number of equations from Section 2. The AM-AFM modality uses only an input drive oscillation to the cantilever and is among the simplest of A-AFM modalities. The calculation of the AM-AFM output signal thus requires relatively few equations from Section 2. The AM-AFM modality may be viewed operationally and analytically as a subset of the RDF-AFUM modality.

3.1 Resonant difference-frequency atomic force ultrasonic microscopy

Resonant difference-frequency atomic force ultrasonic microscopy (RDF-AFUM) employs an ultrasonic wave launched from the bottom of a sample, while the AFM cantilever tip engages the sample top surface. The cantilever is driven at a frequency differing from the ultrasonic frequency by one of the resonance frequencies of the engaged cantilever. It is important to note that at high drive amplitudes of the ultrasonic wave or engaged cantilever (or both) the resonance frequency generating the difference-frequency signal may correspond to one of the nonlinear oscillation modes of the cantilever. The engaged cantilever resonance frequency for the (linear or nonlinear) mode n, neglecting dissipation, is given by $m_c\omega_{cn}^2 = k_{cn} + F'(z_0)k_{cn}[k_s + F'(z_0)]^{-1}$, where k_{cn} is the cantilever stiffness constant corresponding to the nth (linear or nonlinear) non-engaged (free space) resonance mode. Since $F'(z_0)$ may be positive or negative, depending on the shape of the force separation curve, at the separation distance z_0 corresponding to maximum $F''(z_0)$, the resonance frequency of the cantilever, when engaged at this value of z_0, may be larger or

smaller, respectively, than the resonance frequency when not engaged. The nonlinear mixing of the oscillating cantilever and the ultrasonic wave in the region defined by the cantilever tip-sample surface interaction force generates difference-frequency oscillations at the engaged cantilever resonance. Variations in the amplitude and phase of the bulk wave due to the presence of subsurface nano/microstructures, as well as variations in near-surface material parameters, affect the amplitude and phase of the difference-frequency signal. These variations are used to create spatial mappings generated by subsurface and near-surface structures.

In RDF-AFUM the cantilever difference-frequency response is obtained from the nonlinear mixing in the region defined by the tip-surface interaction force. The interaction force varies nonlinearly with the tip-surface separation distance. The deflection of the cantilever obtained in calibration plots is related to this force. For small slopes of the deflection versus separation distance, the interaction force and cantilever deflection curves are approximately related via a constant of proportionality. The maximum difference-frequency signal amplitude occurs when the quiescent deflection of the cantilever is near the bottom of the force-separation curve (z_B in Fig. 2). There the maximum change in the slope of the force versus separation (hence maximum interaction force nonlinearity) occurs. We call this region of operation the maximum nonlinearity regime.

The dominant term or terms for the cantilever difference-frequency displacement in Eqs. (56) and (57) depend on the values of k_{cn} for the free modes of cantilever oscillation, the difference-frequency (ω_c – ω_s), and the value of $F'(z_0)$ obtained at the quiescent separation distance $z_0 = (z_0)B$ at which the maximum difference-frequency signal occurs. We designate the non-engaged linear or nonlinear mode n for which the difference-frequency engaged resonance occurs as n = p. The dominant difference-frequency component in Eqs.(56) and (57) is thus $\eta_{cp} = \eta_{cp,diff} = \zeta_{cp,diff}$ and is given by Eq.(56) for n = p as

$$\zeta_{cp,diff} = G_p \cos[(\omega_c - \omega_s)t - \phi_{cc} + \phi_{ss} + \beta_{cs} - \phi_{cs} + \Gamma - \theta] \tag{69}$$

where Gp is given by Eq.(57) and in approximation by Eq.(66). The phase terms in Eq.(69) are obtained from Eqs. (36), (37), (45), (46), and (62)-(64) where Γ may be approximated by Eq. (66).

It is important to point out in considering these equations that while the difference-frequency resonance frequency $(\omega_c - \omega_s)$ in RDF-AFUM is usually set to correspond to the lowest resonance mode of the engaged cantilever (although a higher modal resonance could be used), the cantilever driving frequency ω_c and ultrasonic frequency ω_s generally are set near (but not necessary equal to) higher resonance modes n = q and n = r, respectively, of the engaged cantilever. Thus, the cantilever stiffness constant k_{cn} is appropriately given as k_{cp} when involving the difference-frequency terms in Eqs. (36)-(39), (42)-(46), and (58)-(64), given as k_{cq} when involving the cantilever drive frequency ω_c at or near the frequency of the qth cantilever resonance mode, and given as k_{cr} when involving the ultrasonic frequency ω_s at or near the frequency of the rth cantilever resonance mode. If ω_c and ω_s are not set at or near a resonance modal frequency of the engaged cantilever, then it may be necessary to include more than one term in Eqs. (12) and (32) corresponding to various values of q and r.

It is seen from Eq. (57) that for a given value of $(\omega_c - \omega_s)$ the maximum value of $\zeta_{cp,diff}$ ideally occurs for a value of z_0 such that $F''(z_0)$ is maximized. It is important to note,

however, that $F'(z_0)$, while relatively small in magnitude compared to that of the hard contact regime, is generally not equal to zero at that point. Strictly, the values of $F''(z_0)$ and $F'(z_0)$ for a given z_0 are each dependent on the exact functional form of $F(z_0)$. A functional form for $F(z_0)$ sufficiently quantitative to quantify $F''(z_0)$ and $F'(z_0)$ is not typically available. However, experimental curves for $F(z_0)$ can be obtained and compared to the experimental curves of $\zeta_{cp,diff}$ plotted as a function of z_0. An examination of Eq. (57) suggests that a more exact approach to maximizing $\zeta_{cp,diff}$ would be not only to vary z_0 but also to vary slightly the difference-frequency from the free space resonance condition until an optimal setting for both z_0 and the difference-frequency is achieved.

3.2 Amplitude modulation-atomic force microscopy

The amplitude modulation-atomic force microscopy (AM-AFM) mode (also called intermittent contact mode or tapping mode) is a standard feature on many atomic force microscopes for which the cantilever is driven in oscillation, but no surface oscillations resulting from bulk ultrasonic waves are generated (i.e., Fs and ω_s are zero). Thus, AM-AFM cannot be used to image subsurface features, but interesting surface properties and features can be imaged. Since AM-AFM can be used in both the hard contact and maximum nonlinearity regimes (i.e. the linear and maximally nonlinear regimes, respectively, of the force-separation curve), the cantilever displacement $\eta_{cn,lin}$ for mode n is given most generally as

$$\eta_{cn.lin} = \xi_{cn} + \zeta_{cn,lin} \tag{70}$$

where ξ_{cn} is given by Eq.(35) with the term involving Q_{cs} set equal to zero and $\zeta_{cn,lin}$ is given by Eq.(47) with all terms involving Q_{cs} and Q_{ss} set equal to zero.

3.2.1 Maximum nonlinearity regime

For the maximum nonlinearity regime the expression for $\eta_{cn,lin}$ is

$$\eta_{cn,lin} = H\cos(\omega_c t - \phi_{cc} + \Lambda) \tag{71}$$

where

$$\Lambda = \tan^{-1}\frac{\sin(\beta_c + \mu_{cc} - \phi_{cc} - \alpha_{cc})}{\cos(\beta_c + \mu_{cc} - \phi_{cc} - \alpha_{cc}) + (Q_{cc}/W)}, \tag{72}$$

$$W = \frac{D_c}{R_{cc}}\varepsilon_0 F''(z_0)(Q_{cc}^2 + Q_{sc}^2 + 2Q_{cc}Q_{sc}\cos\alpha_{cc})^{1/2}, \tag{73}$$

and

$$H = [Q_{cc}^2 + W^2 + 2Q_{cc}W\cos(\beta_c + \mu_{cc} - \phi_{cc} - \alpha_{cc})]^{1/2} \tag{74}$$

where Q_{cc} is given by Eq.(38), Q_{sc} by Eq.(43), ϕ_{cc} by Eq.(36), μ_{cc} by Eq.(48), ε_0 by Eq.(42); a_{cc}, β_c, D_c, and R_{cc}, are given by Eqs.(45), (50), (52), and (53), respectively.

3.2.2 Hard contact regime

The complexity of the cantilever response $\eta_{cn,lin}$ for AM-AFM is greatly reduced for the hard contact regime, where $F''(z_0)$ is negligibly small and $F'(z_0)$ is very large and negative. For sufficiently hard contact Λ and α_{cc} are approximately zero and we obtain from Eq. (71) that

$$\eta_{cn,lin} \approx Q_{cc}\cos(\omega_c t - \phi_{cc}) \tag{75}$$

where

$$Q_{cc} = F_c[(k_{cn} + k_s - m_c\omega_c^2)^2 + (\gamma_c + \gamma_s)^2\omega_c^2]^{-1/2} \tag{76}$$

and

$$\phi_{cc} = \tan^{-1}\frac{(\gamma_c + \gamma_s)\omega_c}{k_{cn} + k_s - m_c\omega_c^2}\,. \tag{77}$$

The dependence of $\eta_{cn,lin}$ on the material damping coefficient γ_s and the sample stiffness constant k_s, both for the hard contact and the maximum nonlinearity regimes, means that AM-AFM can be used to assess the viscoelastic properties of the material irrespective of the regime of operation.

4. Image contrast for representative A-AFM modalities

All the above equations, except for Eqs.(26) - (31), were derived for constant values of the cantilever and material parameters. If, in an area scan of the sample, the parameters remain constant from point to point, the image generated from the scan would be flat and featureless. We consider here that the sample stiffness constant k_s may vary from point to point on the sample surface. Since k_s is dependent on the Young modulus E (see Section 4.3), this means that E also varies from point to point. We assume that the value of the sample stiffness constant k_s' at a given point on the surface differs from the value k_s at another position as $k_s' = k_s + \Delta k_s$. For any function $f(k_s)$ having a functional dependence on k_s, a variation in k_s generates a variation in $f(k_s)$ given by $\Delta f = (df/dk_s)_0\Delta k_s$, where the subscripted zero indicates evaluation at k_s. A similar expression can be obtained for the material damping parameter γ_s, but we shall not consider such variations here.

A variation in k_s produces a variation in both amplitude and phase of the signal generated by the cantilever tip-sample surface interactions. The variations in amplitude and phase can be used to generate amplitude and phase images, respectively, in a surface scan of the sample. We consider here only images generated by the phase variations in the signal. The equations for amplitude-generated images are given elsewhere (Cantrell & Cantrell, 2008). The phase factors involved in RDF-AFUM are given from Eq.(69), (29), and (30) to be ϕ_{cc}, ϕ_{ss}, β_{cs}, ϕ_{cs}, Γ, and χ; the phase factors involved in the AM-AFM mode are, from Eq.(71), ϕ_{cc}, and Λ. Each of these phase factors is dependent on k_s and the variations in the phase factors resulting from variations in k_s are responsible for image generation when using phase detection of the A-AFM signal. The exact dependence of the phase on k_s, however, is different for hard contact and maximum nonlinearity regimes.

4.1 Resonant difference-frequency atomic force ultrasonic microscopy

RDF-AFUM operates only in the maximum nonlinearity regime where the total variation in phase is given as ($\Delta\beta_{cs} + \Delta\phi_{cc} + \Delta\phi_{ss} - \Delta\phi_{cs} + \Delta\Gamma - \Delta\chi$). The phase factors relevant to RDF-AFUM are given as

$$\Delta\beta_{cs} = \left(\frac{d\beta_{cs}}{dk_s}\right)_0 \Delta k_s = -\frac{\gamma_s \Delta\omega}{[k_s + F'(z_0)]^2 + \gamma_s^2(\Delta\omega)^2}\Delta k_s \tag{78}$$

and

$$\Delta\phi_{cc} = -\frac{A_{cc}}{B_{cc}}\Delta k_s \tag{79}$$

where

$$A_{cc} = [\gamma_s k_{cq}^2 + 2F'(z_0)\gamma_s k_{cq} + F'(z_0)^2(\gamma_c + \gamma_s)]\omega_c \tag{80}$$

$$+ [\gamma_c^2\gamma_s - 2\gamma_s m_c(k_{cq} + F'(z_0))]\omega_c^3 + m_c^2\gamma_s\omega_c^5$$

and

$$B_{cc} = \{[\gamma_c k_s + \gamma_s k_{cq} + F'(z_0)(\gamma_c + \gamma_s)]\omega_c - \gamma_s m_c\omega_c^3\}^2 \tag{81}$$

$$+ \{[k_{cq} - m_c\omega_c^2 + F'(z_0)]k_s + F'(z_0)(k_{cq} - m_c\omega_c^2) - \gamma_c\gamma_s\omega_c^2\}^2,$$

$$\Delta\phi_{ss} = -\frac{A_{ss}}{B_{ss}}\Delta k_s \tag{82}$$

where

$$A_{ss} = [\gamma_s k_{cr}^2 + 2F'(z_0)\gamma_s k_{cr} + F'(z_0)^2(\gamma_c + \gamma_s)]\omega_s \tag{83}$$

$$+ [\gamma_c^2\gamma_s - 2\gamma_s m_c(k_{cr} + F'(z_0))]\omega_s^3 + m_c^2\gamma_s\omega_s^5$$

and

$$B_{ss} = \{[\gamma_c k_s + \gamma_s k_{cr} + F'(z_0)(\gamma_c + \gamma_s)]\omega_s - \gamma_s m_c\omega_s^3\}^2 \tag{84}$$

$$+ \{[k_{cr} - m_c\omega_s^2 + F'(z_0)]k_s + F'(z_0)(k_{cr} - m_c\omega_s^2) - \gamma_c\gamma_s\omega_s^2\}^2,$$

and

$$\Delta\phi_{cs} = -\frac{A_{cs}}{B_{cs}}\Delta k_s \tag{85}$$

where

$$A_{cs} = [\gamma_s k_{cp}^2 + 2F'(z_0)\gamma_s k_{cp} + F'(z_0)^2(\gamma_c + \gamma_s)](\Delta\omega) \tag{86}$$

$$+[\gamma_c^2\gamma_s - 2\gamma_s m_c(k_{cp} + F'(z_0))](\Delta\omega)^3 + m_c^2\gamma_s(\Delta\omega)^5$$

and

$$B_{cs} = \{[\gamma_c k_s + \gamma_s k_{cp} + F'(z_0)(\gamma_c + \gamma_s)](\Delta\omega) - \gamma_s m_c(\Delta\omega)^3\}^2 \tag{87}$$

$$+\{[k_{cp} - m_c(\Delta\omega)^2 + F'(z_0)]k_s + F'(z_0)[k_{cp} - m_c(\Delta\omega)^2] - \gamma_c\gamma_s(\Delta\omega)^2\}^2 .$$

To the extent that $\Gamma = \alpha_{cc} - \alpha_{ss}$, as given by Eq.(65), we may write

$$\Delta\Gamma = \Delta\alpha_{cc} = -\frac{\gamma_s\omega_c}{[k_s + F'(z_0)]^2 + \gamma_s^2\omega_c^2}\Delta k_s . \tag{88}$$

The phase term $\Delta\chi$ is given by Eqs. (22) and (31).

4.2 Amplitude modulation-atomic force microscopy

The appropriate variations in the phase factors relevant to the AM-AFM or tapping mode maximum nonlinearity regime are $\Delta\alpha_{cc}$, $\Delta\phi_{cc}$, and $\Delta\Lambda$. The factor $\Delta\Lambda$ is obtained from Eq.(72) as

$$\Delta\Lambda = \frac{1 + (Q_{cc}/W)\cos(\beta_c + \mu_{cc} - \phi_{cc} - \alpha_{cc})}{[\cos(\beta_c + \mu_{cc} - \phi_{cc} - \alpha_{cc}) + (Q_{cc}/W)]^2 + \sin^2(\beta_c + \mu_{cc} - \phi_{cc} - \alpha_{cc})} \tag{89}$$

$$\times(\Delta\beta_c + \Delta\mu_{cc} - \Delta\phi_{cc} - \Delta\alpha_{cc})$$

where

$$\Delta\beta_c = -\frac{\gamma_s\omega_c}{k_s^2 + \gamma_s^2\omega_c^2}\Delta k_s , \tag{90}$$

$\Delta\phi_{cc}$ is given by Eq. (79), and $\Delta\mu_{cc}$ is obtained from Eq.(48). To the extend that Q_{sc} is much smaller than Q_{cc}, we get from Eq. (48) that $\Delta\mu_{cc} = \Delta\alpha_{cc}$ where $\Delta\alpha_{cc}$ is given by Eq. (88).
For the hard contact regime where $F'(z_0)$ is very large and negative, the relevant phase variation is obtained from Eq. (77) as

$$\Delta\phi_{cc} = -\frac{(\gamma_c + \gamma_s)\omega_c}{(k_s + k_{cq} - m_c\omega_c^2)^2 + (\gamma_c + \gamma_s)^2\omega_c^2}\Delta k_s . \tag{91}$$

As a word of caution, the extent to which the hard contact equation applies depends on how well the approximation $F'(z_0) \to -\infty$ holds. In those cases where such an assumption is suspect, the equations for the maximum nonlinearity regime should be used.

4.3 Dependence on the Young modulus

Hertzian contact theory provides that the sample stiffness constant k_s is related to the Young modulus E of the sample as (Yaralioglu et al., 2000)

$$k_S = 2r_c\left(\frac{1-\upsilon_T^2}{E_T}+\frac{1-\upsilon^2}{E}\right)^{-1} \tag{92}$$

where υ is the Poisson ratio of the sample material, E_T and υ_T are the Young modulus and Poisson ratio, respectively, of the cantilever tip, and r_c is the cantilever tip-sample surface contact radius. Hence,

$$\Delta k_S = \frac{2r_c\left(1-\upsilon^2\right)}{E^2}\left(\frac{1-\upsilon_T^2}{E_T}+\frac{1-\upsilon^2}{E}\right)^{-2}\Delta E = \frac{k_S}{E}(1-\nu^2)\left(\frac{1-\upsilon_T^2}{E_T}+\frac{1-\upsilon^2}{E}\right)^{-1}\frac{\Delta E}{E}. \tag{93}$$

Strictly, Eq. (93) was derived for the case of repulsive interaction forces leading to a concave elastic deformation of a flat sample surface from a contacting hard spherical object. However, we consider here that to a crude approximation Eqs. (92) and (93) also hold for attractive interactive forces providing that the elastic deformation of the sample surface is viewed as a convex deformation (asperity) subtending an effective contact radius r_c with the cantilever tip that is appropriately different in magnitude from that of the repulsive force case. As pointed out in Section 2.3.3, the cantilever oscillations are known to be bi-stable with the particular mode of oscillation being determined by the initial conditions that includes the tip-surface separation distance. In the present model the bi-stable mode of cantilever oscillation is set by the value of the "effective" sample stiffness constant k_s corresponding either to the dominantly repulsive region or dominantly attractive region of the force-separation curve.

Eq. (93) can be used with Eqs. (78)-(91) to ascertain the fractional variation in the Young modulus $\Delta E/E$ from measurements of the phase variation in the signal from an appropriate A-AFM modality. For the case where $E_T >> E$, e.g. for polymeric or soft biological materials, Eq. (92) reduces to $k_s = 2r_cE$ and Eq. (93) reduces to $\Delta k_s = k_s(\Delta E/E)$.

5. Assessment of model validity

We assess the validity of the above analytical model by comparing variations in the Young modulus of a specimen as calculated from the model with independent experimental measurements of the same specimen material. The choice of material is influenced by a recent focus to develop high performance polymers having low density, high strength, optical transparency, and high radiation resistance for a variety of applications in hostile space environments. One such polymer is LaRC™-CP2 polyimide. We consider here the application of RDF-AFUM and AM-AFM to assess variations in the Young modulus of nancomposites composed of nanoparticles embedded in a LaRC™-CP2 polyimide matrix. We consider two nanocomposites – one embedded with gold nanoparticles and the other embedded with single wall carbon (SWCNT) nanotube bundles.

We first consider a specimen of LaRC™-CP2 polyimide polymer roughly 12.7 μm thick containing a monolayer of randomly distributed gold particles, roughly 10-15 nm in diameter and embedded roughly 7 μm beneath the specimen surface. Fig. 5a is an AM-AFM

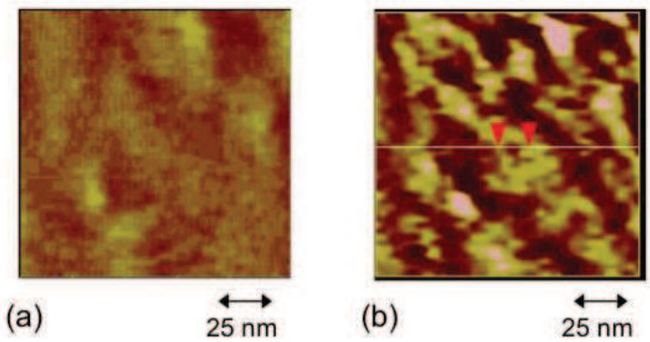

Fig. 5. Micrographs of LaRC™-CP2 polyimide polymer embedded with gold nanoparticles. (a) Noncontact tapping mode (AM-AFM) phase-generated micrograph. (b) RDF-AFUM phase-generated image over the same scan area as (a). (from Cantrell et al., 2007)

phase-generated image obtained in the maximum nonlinearity regime (noncontact tapping mode). A commercial cantilever having a stiffness constant of 14 N m^{-1}, a lowest-mode resonance frequency of 302 kHz, and a cantilever damping coefficient of roughly 10^{-8} kg s^{-1} is driven at 2.1 MHz to obtain the micrograph of Fig.5a (Cantrell et al., 2007). The values of the relevant model parameters for LaRC™-CP2 polyimide polymer are 1.4 x 10^3 kg m^{-3} for the mass density ρ, 2.4 GPa for the Young modulus E, 0.37 for the Poisson ratio υ, k_s = 96.1 N m^{-1}, and γ_s = 4.8 x 10^{-5} kg s^{-1} (Park et al., 2002; Fay et al., 1999; Cantrell et al. 2007). Since no bulk ultrasonic wave is involved, the image contrast results only from variations in the specimen near-surface sample stiffness constant k_s. The darker areas in the image correspond to larger values of the sample stiffness constant, hence Young modulus, relative to that of the brighter areas. The maximum phase difference between the bright and dark areas in the image is approximately 1.5 degrees. Using the value 1.5 degrees, we obtain from the model that the variation in the Young modulus $\Delta E/E \approx 18\%$. This value is consistent with the value $\Delta E/E \approx 21\%$obtained from independent mechanical stretching experiments on pure LaRC™-CP2 polymer sheets (Fay et al., 1999).

An RDF-AFUM phase image of the same scan area as that of Fig. 5a is shown in Fig. 5b. The RDF-AFUM image reveals bright and dark regions over the scan area that broadly correspond to the bright and dark regions in the surface image of Fig. 5a, although the image contrast and local detail appears to differ in the two images. F′(z) is assessed to be roughly –53 N m^{-1} at the tip-surface separation corresponding to the maximum difference-frequency signal. The acoustic wave has a frequency of 1.8 MHz. The maximum variation in phase shown in Fig.5b is approximately 13.2 degrees. Using the value 13.2 degrees, we obtain from the model that the variation in the Young modulus $\Delta E/E \approx 24\%$. This value is also consistent with the value $\Delta E/E \approx 21\%$obtained from independent mechanical stretching experiments on pure LaRC™-CP2 polymer sheets.

The existence of contiguous material with differing elastic constants suggests that the LaRC™-CP2 material is not homogeneous. The broad coincidence of dark (bright) regions in the images of Fig.5a and 5b suggests that the polymer structure giving rise to a larger (smaller) elastic modulus in the bulk material occurs in varying amounts through the bulk to the surface, the degree of darkness (brightness) in Fig. 5b being somewhat reflective of the

structural homogeneity of the material along the propagation path of the ultrasonic wave. It is assumed that the appearance of contiguous material with different elastic coefficients may result from the growth of a strain-nucleated harder material phase resulting from the difference in the coefficients of thermal expansion between the polymer matrix and the embedded gold particles.

To test the assumption of a strain-nucleated harder phase, micrographs were obtained of a specimen formed from bundles of single-wall carbon nanotubes (SWCNTs) distributed randomly through the bulk of a 50μm-thick film of LaRC™-CP2 polymer. Figure 6a shows a conventional atomic force microscope (AFM) topographical image of the specimen showing only surface features. A RDF-AFUM phase-image of the specimen, taken in the same scan area as that of Fig 6a, is shown in Fig. 6b. Comparison of the two images reveals the appearance of subsurface bundles of SWCNTs (dark contrast filamentary features) lying in the plane of the RDF-AFUM image that do not appear in the AFM topographical scan. Dramatic variations from dark to bright to slightly bright contrast occur in image plane along portions of the boundary between the bundles of SWCNTs and the matrix material. The variations follow the contour of the nanotube bundles and suggest the occurrence of an interphase region (bright contrast feature) at the nanotube bundle-polymer interface. The interphase consists of polymer material having dramatically different mechanical properties from that of the matrix material. We note, however, that aside from the local interphase regions in Fig. 6b there are no broad, contiguous regions of material with differing elastic constants as observed in Fig. 5. Since the difference between the coefficients of thermal expansion of LaRC™-CP2 polymer and SWCNT bundles is considerable less than that for LaRC™-CP2 polymer and gold particles, we infer that the thermal strains in SWCNT bundle-embedded polymer material are not sufficiently large to generate the larger contiguous features observed in material embedded with gold particles.

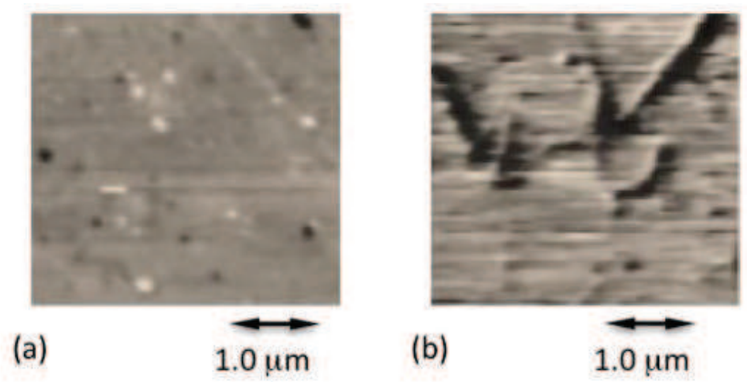

Fig. 6. Micrographs of LaRC™-CP2 polyimide polymer embedded with single wall carbon nanotube bundles. (a) AFM topographical image. (b) RDF-AFUM phase-generated image over the same scan area as (a).

6. Conclusion

The various dynamical implementations of the atomic force microscope have become important nanoscale characterization tools for the development of novel materials and devices. One of the most significant factors affecting all dynamical AFM modalities is the cantilever tip-sample surface interaction force. We have developed a detailed mathematical model of this interaction that includes a quantitative consideration of the nonlinearity of the interaction force as a function of the cantilever tip-sample surface separation distance. The model makes full use of cantilever beam dynamics and the multiply differentiability of the continuous force-separation curve that results in a set of coupled differential equations, Eqs.(14) and (15), for the displacement amplitudes of both the cantilever and the sample surface. The coupled dynamical equations are recast in matrix form and solved by a standard iteration procedure, but space limitations allow only a presentation of the salient features of the procedure. Although the mathematical form of the coupled equations are valid for any vibrational mode, only flexural vibrations of the cantilever and out-of-plane oscillations of the sample surface are considered.

We emphasize that Eqs.(14) and (15) are obtained assuming that the cantilever is a rectangular beam of constant cross-section, the dynamics of which are characterized by a set of eigenfunctions that form an orthogonal basis for the solution set. For some other cantilever shape a different orthogonal basis set of eigenfunctions would be appropriate. However, the mathematical procedure used here would lead again to Eqs.(14) and (15) with values of the coefficients appropriate to the different cantilever geometry. Practicably, this means that the shape of the cantilever is not as important in the solution set as knowing the cantilever modal resonant frequencies, obtained experimentally. The modal frequencies and solution set are expanded to include nonlinear modes generated by nonlinear interaction forces or large cantilever drive amplitudes.

A general steady state solution of the coupled dynamical equations is found that accounts for the positions of the excitation force (e.g., a piezo-transducer) and the cantilever tip along the length of the cantilever and for the position of the laser probe on the cantilever surface. The solution is applied to two dynamical AFM modalities - resonant difference-frequency atomic force ultrasonic microscopy, and the commonly used amplitude modulation-atomic force microscopy. Image generation and contrast equations are obtained for each of the two A-AFM modalities assuming for expediency that the contrast results only from variations in the sample stiffness constant. Since the sample stiffness constant is related directly to the Young modulus of the sample, the contrast can be expressed in terms of the variation in the Young modulus from point to point as the sample is scanned. We note further the existence of two values of the sample stiffness constant, corresponding to the dominantly attractive and dominantly repulsive regimes of the force-separation curve. The two values allow for a bi-stability in the cantilever oscillations that is experimentally observed.

Equations for both the maximum nonlinearity regime and the hard contact (linear) regime of cantilever engagement with the sample surface are obtained. For dynamical AFM operation outside these regimes, it is necessary to use all terms in the solution set given in Section 2 to describe the signal output of a given A-AFM modality. The extent to which the hard contact (linear regime) equations apply depends on how well the approximation $F'(z_0) \to -\infty$ holds.

In those cases where such an assumption is suspect, all terms in the equations for a given modality should be used.

In order to test the validity of the present model, comparative measurements of the fractional variation of the Young modulus $\Delta E/E$ in a film of LaRC™-CP2 polyimide polymer were obtained from phase-generated images obtained over the same scan area of the specimen using the RDF-AFUM and AM-AFM maximum nonlinearity modalities. The two modalities represent opposite extremes in measurement complexity, both in instrumentation and in the analytical expressions used to calculate $\Delta E/E$. The values 24 percent calculated for RDF-AFUM and 18 percent calculated for the AM-AFM maximum nonlinearity mode are in remarkably close agreement for such disparate techniques. The agreement of both calculations with the value of 21 percent obtained from independent mechanical stretching experiments of LaRC™-CP2 polymer sheet material offers strong evidence for the validity of the present model.

The present model can also be used to quantify the image contrast from variations in the sample damping coefficient γ_S in the material. Space limitations prohibit the inclusion of such contrast mechanisms here, but the effects can be derived straightforwardly by the reader from the equations derived in Section 2. Although the present model is developed for flexural oscillations of the cantilever and out-of-plane vibrations of the sample surface, the model can be extended to include other modes of cantilever oscillation and sample surface response as well.

7. References

Binnig, G; Quate, C. F. & Gerber, Ch. (1986). Atomic force microscope. *Physical Review Letters*, 56, 930-933.

Bolef, D. I. & and J. G. Miller, J. G. (1971). High-frequency continuous wave ultrasonics. In: *Physical Acoustics, Vol. VIII*, W. P. Mason and R. N. Thurston, Ed., Academic, New York, 95-201.

Cantrell, J. H. (2004). Determination of absolute bond strength from hydroxyl groups at oxidized aluminum-epoxy interfaces by angle beam ultrasonic spectroscopy. *Journal of Applied Physics*, 96, 3775-3781.

Cantrell, S. A.; Cantrell, J. H. & Lillehei, P. T. (2007). Nanoscale subsurface imaging via resonant difference-frequency atomic force ultrasonic microscopy. *Journal of Applied Physics*, 101, 114324.

Cantrell, J.H. & Cantrell, S. A. (2008). Analytical model of the nonlinear dynamics of cantilever tip-sample surface interactions for various acoustic atomic force microscopies. *Physical Review B*, 77, 165409.

Chan, H. B.; Aksyuk, V. A.; Kleiman, R. N.; Bishop, D. J. & Capasso, F. (2001). Nonlinear micromechanical Casimir oscillator. *Physical Review Letters*, 97, 211801.

Cuberes, M. T.; Alexander, H. E.; Briggs, G. A. D. & and Kolosov, O. V. (2000). Heterodyne force microscopy of PMMA/rubber nanocomposites: nanomapping of viscoelastic response at ultrasonic frequencies. *Journal of Physics D: Applied Physics*, 33, 2347-2355.

Cuberes, M. T. (2009). Intermittent-contact heterodyne force microscopy. *Journal of Nanomaterials*, 2009, 762016.

Eguchi, T. & Hasegawa, Y. (2002). High resolution atomic force microscopic imaging of the Si(111)-(7x7) surface: contribution of short-range force to the images. *Physical Review Letters*, 89, 266105.

Fay, C. C.; Stoakley, D. M. & St. Clair, A. K. (1999). Molecularly oriented films for space applications. *High Performance Polymers*, 11, 145-156.

Garcia, R & Perez, R. (2002). Dynamic atomic force microscopy methods. *Surface Science Reports*, 47, 1-79.

Geer, R. E.; Kolosov, O. V.; Briggs, G. A. D. & Shekhawat, G. S. (2002). Nanometer-scale mechanical imaging of aluminum damascene interconnect structures in a low-dielectric-constant polymer. *Journal of Applied Physics*, 91, 9549-4555.

Hölscher, H.; Schwarz, U. D. & Wiesendanger, R. (1999). Calculation of the frequency shift in dynamic force microscopy. *Applied Surface Science*, 140, 344-351.

Hurley, D. C.; Shen, K.; Jennett, N. M. & Turner, J. A. (2003). Atomic force acoustic microscopy methods to determine thin-film elastic properties. *Journal of Applied Physics*, 94, 2347-2354.

Kokavecz, J.; Marti, O.; Heszler, P. & and Mechler, A. (2006). Imaging bandwidth of the tapping mode atomic force microscope probe. *Physical Review B*, 73, 155403.

Kolosov O. & Yamanaka, K. (1993). Nonlinear detection of ultrasonic vibrations in an atomic force microscope. *Japanese Journal of Applied Physics*, 32, L1095-L1098.

Kolosov, O. V.; Castell, M. R.; Marsh, C. D.; Briggs, G. A. D.; Kamins, T. I. & Williams, R. S. (1998). Imaging the elastic nanostructure of Ge islands by ultrasonic force microscopy. *Physical Review Letters*, 81, 1046-1049.

Kopycinska-Müller, M.; Geiss, R. H. & Hurley, D. C. (2006). Contact mechanics and tip shape in AFM-based nanomechanical measurements. *Ultramicroscopy* 106, 466-474.

Lantz, M. A.; Hug, H. J.; Hoffmann, R.; van Schendel, P. J. A.; Kappenberger, P.; Martin, S.; Baratoff, A. & Güntherodt, H.-J. (2001). Quantitative measurtement of short-range chemical bonding forces. *Science*, 291, 2580-2583.

Law, B. M. & Rieutord, F. (2002). Electrostatic forces in atomic force microscopy. *Physical Review B*, 66, 035402.

Lee, H.-L.; Yang, Y.-C.; Chang, W.-J. & Chu, S.-S. (2006). Effect of interactive damping on vibration sensitivities of V-shaped atomic force microscope cantilevers. *Japanese Journal of Applied Physics,* 45, 6017-6021.

Maivald, P.; Butt, H. J.; Gould, S. A.; Prater, C. B.; Drake, B.; Gurley, J. A.; Elings, V. B. & Hansma, P. K. (1991). Using force modulation to image surface elasticities with the atomic force microscope. *Nanotechnology*, 2, 103-106.

Meirovitch, L. (1967). *Analytical Methods in Vibrations*, Macmillan, New York.

Muthuswami, L. & Geer, R. E. (2004). Nanomechanical defect imaging in premetal dielectrics for integrating circuits. *Applied Physics Letters*, 84, 5082-5084.

Nony, L.; Boisgard, R. & Aime, J. P. (1999). Nonlinear dynamical properties of an oscillating tip-cantilever system in the tapping mode. *Journal of Chemical Physics*, 111, 1615-1627.

Park, C.; Ounaies, Z.; Watson, K. A.; Crooks, R. E.; Smith, Jr., J.; Lowther, S. E.; J. Connell, W.; Siochi, E. J.; Harrison, J. S. & St. Clair, T. L. (2002). Dispersion of single wall carbon nanotubes by in situ polymerization under sonication. *Chemical Physics Letters*, 364, 303-308.

Polesel-Maris, J; Piednoir, A.; Zambelli, T.; Bouju, X. & Gauthier, S. (2003). Experimental investigation of resonance curves in dynamic force microscopy. *Nanotechnology*, 14, 1036-1042.

Rabe U. & Arnold, W. (1994). Acoustic microscopy by atomic force microscopy. *Applied Physics Letters*, 64, 1493-1495.

Rabe, U.; Amelio, S.; Kopychinska, M.; Hirsekorn, S.; Kempf, M.; Goken, M. & Arnold, W. (2002). Imaging and measurement of local mechanical properties by atomic force micrscopy. *Surface and Interface Analysis*, 33, 65-70.

Saint Jean, M.; Hudlet, S.; Guthmann, C. & Berger, J. (1994). Van der Waals and capacitive forces in atomic force microscopies. *Journal of Applied Physics*, 86, 5245-5248.

Schiff, L. I. (1968). *Quantum Mechanics*, McGraw-Hill, New York.

Shekhawat, G. S. & Dravid V. P. (2005). Nanoscale imaging of buried structures via scanning near-field ultrasonic holography. *Science*, 310, 89-92.

Sokolnikoff, I. S. & Redheffer, R. M. (1958). *Mathematics of Physics and Modern Engineering*, McGraw-Hill, New York.

Stark, R. W. & Heckl, W. M. (2003). Higher harmonics imaging in tapping-mode atomic-force microscopy. *Review of Scientific Instruments*, 74, 5111-5114.

Stark, R. W.; Schitter, G.; Stark, M.; Guckenberger, R. & Stemmer, A. (2004). State-space model of freely vibrating surface-coupled cantilever dynamics in atomic force microscopy. *Physical Review B*, 69, 085412.

Turner, J. A. (2004). Nonlinear vibrations of a beam with cantilever-Hertzian contact boundary conditions. *Journal of Sound and Vibration*, 275, 177-191.

Überall, H. (1997). Interference and steady-state scattering of sound waves. In: *Encyclopedia of Acoustics*, *Vol. 1*, Malcohm J. Crocker, (Ed.), 55-68, Wiley, ISBN 0-471-17767-9, New York.

Wolf, K. & Gottlieb, O. (2002). Nonlinear dynamics of a noncontacting atomic force microscope cantilever actuated by a piezoelectric layer. *Journal of Applied Physics*, 91, 4701-4709.

Yagasaki, K. (2004). Nonlinear dynamics of vibrating microcantilevers in tapping-mode atomic force micrscopy. *Physical Review B*, 70, 245419.

Yamanaka, K.; Ogiso, H. & Kolosov, O. (1994). Ultrasonic force microscopy for nanometer resolution subsurface imaging. *Applied Physics Letters*, 64, 178-180.

Yaralioglu, G. G.; Degertekin, F. L.; Crozier, K. B. & Quate, C. F. (2000). Contact stiffness of layered materials for ultrasonic atomic force microscopy. *Journal of Applied Physics*, 87, 7491-7496.

Zheng, Y.; Geer, R. E.; Dovidenko, K.; Kopycinska-Müller, M. & Hurley, D. C. (2006). Quantitative nanoscale modulus measurements and elastic imaging of SnO_2 nanobelts. *Journal of Applied Physics*, 100, 124308.

Zhong , Q.; Inniss, D.; Kjoller, K. & Elings, V. B. (1993). Fractured polymer/silica fiber surface studied by tapping mode atomic force microscopy. *Surface Science Letters*, 290, L688 – L692.

Nonlinear Dynamics

Edited by Todd Evans

ISBN 978-953-7619-61-9
Hard cover, 366 pages
Publisher InTech
Published online 01, January, 2010
Published in print edition January, 2010

This volume covers a diverse collection of topics dealing with some of the fundamental concepts and applications embodied in the study of nonlinear dynamics. Each of the 15 chapters contained in this compendium generally fit into one of five topical areas: physics applications, nonlinear oscillators, electrical and mechanical systems, biological and behavioral applications or random processes. The authors of these chapters have contributed a stimulating cross section of new results, which provide a fertile spectrum of ideas that will inspire both seasoned researches and students.

InTech Europe
University Campus STeP Ri
Slavka Krautzeka 83/A
51000 Rijeka, Croatia
Phone: +385 (51) 770 447
Fax: +385 (51) 686 166
www.intechopen.com

InTech China
Unit 405, Office Block, Hotel Equatorial Shanghai
No.65, Yan An Road (West), Shanghai, 200040, China
中国上海市延安西路65号上海国际贵都大饭店办公楼405单元
Phone: +86-21-62489820
Fax: +86-21-62489821

IntechOpen